Characterization and Modeling of Failure Initiation in Bainite-Aided DP Steel**

By *Ali Ramazani,** Yuling Chang* and *Ulrich Prahl*

This research work aims to characterize and model the failure initiation in bainite-aided dual-phase (DP) steel. Combined electron backscatter diffraction (EBSD) and electron probe microanalysis (EPMA) measurements were applied to quantify the constituents (ferrite, martensite, and bainite) in the microstructure. Mini tensile test with digital image correlation (DIC) analysis was carried out and linked to local scanning electron microscopy (SEM) analysis to identify macroscopic failure initiation strain values. SEM measurements showed that the crack initiation occurs in martensite islands. A microstructure-based approach by means of representative volume elements (RVE) modeling combined with extended finite element method (XFEM) was utilized to model martensite cracking on mesoscale. The identified parameters were validated by comparing the predictions with the experimental results.

1. Introduction

Since dual-phase (DP) steels show a combination of the high strength with good ductility, they are widely used in the automobile industry.[1] These good properties are attributed to the microstructure of DP steel, which normally consisted of hard martensite particles dispersing in a soft ferrite matrix.[2] Bainite can also be formed in DP steel due to improper industrial heat treatments. Since the mechanical and failure behavior of DP steels, it significantly depends on the microstructure of these materials. Presence of bainite in the microstructure, affects the mechanical behaviors of DP steels as well.[3]

Many researchers investigated the effect of bainite content on the ferrite–bainite–martensite steels.[4–6] Sudo and Iwai[4] indicated that reducing the bainite content in ferrite–bainite–martensite steels causes a decrease of the ratio between the

tensile and yield strength but an increase in the percentage elongation and strain hardening exponent. Kim et al.[5] suggested that small amounts of bainite in ferrite–martensite DP steels lead to an increased yield strength and ductility but it also decreases the tensile strength. Matlock et al.[6] investigated the effect of the microstructure on the mechanical properties of micro-alloyed ferrite–bainite–martensite steels and reported inferior tensile properties and toughness for these steels in comparison to conventional steels.

Application of DP steels is restricted due to their complex failure behavior, which depends on the microstructure of these materials. Therefore, many research works are recently conducted to study failure behavior of DP steels. DP steel fails in a ductile manner, which can be divided into three stages: void nucleation, void growth, and void coalescence. Until now, mainly three observations in the fracture of DP steels have been proved: voids formation because of the brittle fracture of martensite; interface decohesion between martensite and ferrite, and the ductile failure of ferrite matrix.[7–11] Even though at macroscopic scale, DP steel exhibits uniform and homogenous deformation, but due to its grain level inhomogeneity, the microscopic deformation is instable. Shen et al.[8] used a scanning electron microscope (SEM) equipped with a tensile straining stage to illustrate the inhomogeneous strain distribution between ferrite and the martensite grains in DP steels. According to their investigation, the ferrite phase starts to deform immediately and at a much higher rate than the delayed deformation of martensite phase, so the volume percentage of martensite in the DP steel will influence the failure mechanism. Maire et al.[12] investigated the failure behavior of DP steels based on the situ tensile tests. In their

[*] A. Ramazani
Department of Materials Science and Engineering, University of Michigan, 2300 Hayward St., Ann Arbor, MI 48109, USA
E-mail: ramazani@umich.edu
A. Ramazani, Y. Chang, U. Prahl
Department of Ferrous Metallurgy, RWTH Aachen University, Intzestr.1 D-52072 Aachen, Germany

study, X-ray tomography has been used to quantify the evolution of damage. They observed both martensite cracking and ferrite/martensite interface debonding during the test. Tasan[13] have recently stated the fact that there are some other mechanisms that are acting in parallel to the simple damage mechanism. Among these mechanisms, the strain localization and shear banding attracted the most attention.

He et al.[14] studied the fracture mechanism in fine and coarse martensite morphology with 0.09 and 17% martensite. Their results indicated that with coarse martensitic structure, the initial void formation occurs due to cracking of the martensite, followed by the interfacial decohesion at the ferrite/martensite interface. On the contrary, the finely dispersed martensite microstructure, the voids mainly formed in the interface of the martensite/ferrite. Kim and Thomas[15] have reported that the formation of voids in DP steels depends on the morphology of the martensite. For coarse martensite distribution, the failure occurs by cleavage, while for globular and finely distributed martensite, the void initiation occurs at the ferrite–martensite interface and does not occur at the martensite particles. Calcagnotto et al.[16] investigated failure behavior of DP steels with different grain sizes. Their research showed that while in classical DP steels (of coarse grain and high impurity) the cleavage fracture and grain split cause failure, while in modern DP steels (of fine grain and low impurity) grain boundaries play the significant role.

Recently, failure modeling in DP steels is a subject of interest for several research groups[17–25]. They approach the topic through different scientific methods. Sun et al.[17] and Choi et al.[18] studied the failure mode and ultimate ductility of DP steels using a microstructure-based model in different loading and boundary conditions. In their studies, ductile failure was predicted as the result of plastic instability in the form of strain localization triggered by the microstructure-level inhomogeneity between the hard martensite and ferrite phases. Uthaisangsuk et al.[19] investigated the failure of DP steels using RVE approach. They utilized a cohesive zone and Gurson–Tvergaard–Needleman model (GTN) models to study the ferrite–martensite debonding and ferrite degradation, respectively. Vajragupta et al.[20] utilized XFEM with traction separation law and damage curve to study martensite cracking and ferrite degradation in DP steels, respectively. By combining these two damage models in the RVE model on microscopic scale, they investigated different failure modes in DP steels.

Ramazani et al.[21,22] characterized and modeled the failure initiation in DP steel with 46% martensite using XFEM. They carried out in situ bending test with EBSD measurements before and after the test. They also performed a mini tensile test with digital image correlation (DIC) analysis in order to characterize failure initiation in DP steel. In situ analysis of bending test in large-chamber SEM (LC-SEM), which is combined with electron backscatter diffraction (EBSD) measurements, in a conventional field-emission gun SEM (FEG-SEM), before and after the test showed that crack

initiation occurs in martensite islands and during plain stress condition.

The current research work aims to characterize and model the failure initiation in the bainite-aided DP steel. Mini tensile test with DIC technique was carried out to identify responsible local macro strain for martensite cracking, which was considered as boundary condition in microstructure calculation. 2D representative volume elements (RVE) were defined based on real micrographs. The flow behavior of single phases was modeled using a dislocation density based Kocks–Mecking type work-hardening approach. Extended finite element method (XFEM) with traction–separation law (TSL) was locally utilized to model the martensite cracking type failure initiation in bainite-aided DP steels. The failure strain in martensite was identified from 2D RVE simulations, using first order homogenization and based on mini tensile results. The identified parameters were validated by comparing the predictions of microstructure deformation during tensile test with the experimental results from SEM analysis.

2. Experimental Section

2.1. Materials

The material used in this study is a commercial DP steel (DP-K34/60+Z). It was cold-roll-annealed to a thickness of 1.5 mm, as shown in Figure 1. The nominal chemical composition is presented in Table 1.

2.2. Quantification of Microstructure Using Combined EBSD and EPMA

EBSD mappings were performed on a field-emission SEM equipped with a Hikari camera and TSL OIM software to characterize the microstructure of the studied material. The phase identification was improved and validated by measuring the spatial distribution of carbon using electron probe microanalysis (EPMA) measurement. A Schottky field-emission gun electron microprobe was utilized to characterize
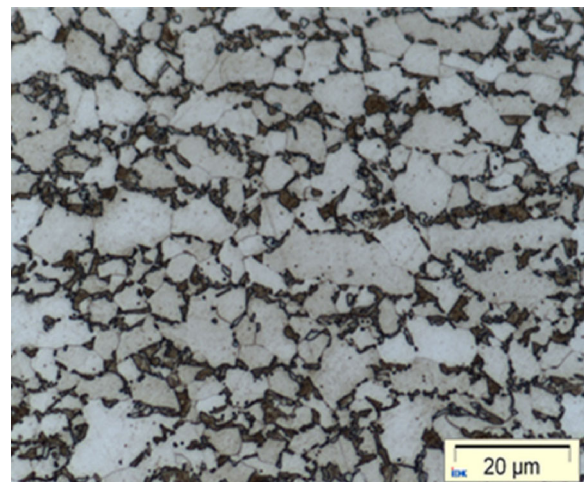

Fig. 1. LOM image of DP steel consisting of ferrite (light areas) and martensite/bainite (dark areas).

FULL PAPER

Table 1. Chemical composition of the investigated DP steel (wt%).

C	Si	Mn	P	Cr	Mo	Al
0.09	0.2	1.24	0.013	0.18	0.2	0.026

and to show carbon content in the microstructures. Based on the characterization result, the final segment of the microstructure can be identified. The elaborated details of the combined EBSD and EPMA techniques are given in ref.[26]

2.3. Uniaxial Tensile Test and Fractography

Tensile samples were cut from the sheet, according to ISO 6892-1. The sample geometry that was utilized for mechanical testing is shown in Figure 2. Three tensile tests were performed parallel to the cold-rolling direction at a velocity of 4 mm min^{-1} at the Zwick 100.

After the tensile test fractography was done on the fracture surface of the samples, the fracture tensile specimens were first the longitudinal direction and then quantitatively analyzed after being polished.

2.4. Mini Tensile Test with Digital Correlation (DIC) Technique

To clarify the local strain and the position of the failure initiation, DP steels, mini tensile test with DIC technique was utilized on the studied bainite-aided DP steel. The geometry and dimensions of tensile test specimen is illustrated in Figure 3.

DIC is an advanced non-contact optical technique for the strain and displacement measurement.[27] In order to have accurate grid of computational assessment, the black areas development pattern should be small, but at the same time we should consider the fact that it should be small but large enough to be completely assessed based on the camera resolution factors associated with it. Moreover to be accurately tested, the sample should not include continuing bright spots in the pattern.[28,29] Within the deformation, various images of the pattern components were taken, analyzed, and compared. However, the selected area is illustrated in Figure 4. Moreover, due to brightness and
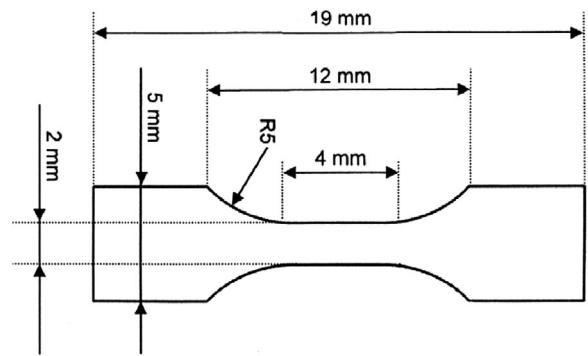
Fig. 3. Geometry and dimensions of the mini tensile specimen for DIC evaluation.

shading limitations, the assessed areas were a little smaller compared to the width of the extensometer.

After tensile testing conventional W-Gun SEM was performed on both sides of prepared fracture surfaces. The acceleration voltage was 25 kV. The working distance was 10–12 mm. The loaded and failed specimen was cut along loading direction in the center line. Here, the microstructure evolution by means of SEM was analyzed to observe where the crack initiates and to match with local strain measurement by DIC data. It helps to identify the dominant failure mechanism and to quantify the critical initiation strain. After cutting, the investigated surface of the specimen was polished mechanically with diamond paste and followed by electro polishing. After etching, the microstructures were observed with a conventional W-gun SEM (DSM 962 by Zeiss). SEM images were taken at various positions, which were selected at different distances from fracture surface (Figure 5). The etching was applied via the method of 3% $Na_2S_2O_5$ for 30 s.

3. Micromechanical Modeling

3.1. RVE Generation

In a former study, the size and number of constituents in an RVE as well as the mesh size influence were identified.[30,31] According to this approach, a 2D RVE from the real microstructures of bainite-aided DP steel was created. To make the RVE from the EBSD/EPMA segmented microstructure (Figure 6a), the meshing program OOF, Version 2.4, 2007,
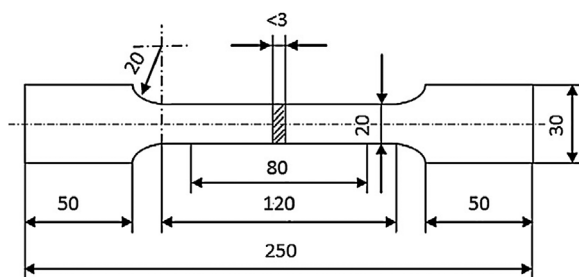
Fig. 2. Sample geometry for standard tensile testing (dimensions are given in mm).
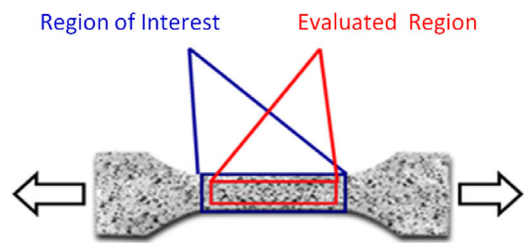
Fig. 4. Area of interest and area of DIC evaluation on the mini tensile sample.
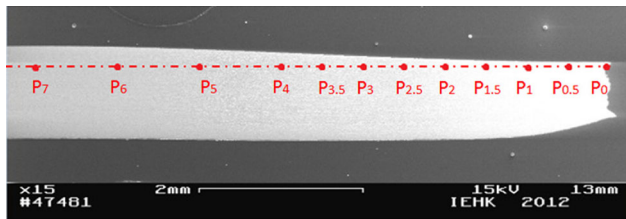
Fig. 5. Positions of SEM analysis in center line of broken mini tensile specimen.

was used (http://www.ctcms.nist.gov/oof/). Quadraticelements with parabolic form functions were used. The generated RVE based on the real microstructures of the developed DP steel is shown in Figure 6b. Periodic boundary conditions using a developed FORTRAN-based program were imposed on the RVE.

3.2. Single Phase Flow Curve Modeling

In the current work, the elastic modulus for ferrite and martensite is assumed to be 210 GPa.[31] The flow curves of ferrite and martensite are quantified based on a dislocation-based strain hardening model.[32] This model emerges from the classical dislocation theory approach of refs.[33,34] and from the work of ref.[35] The model constants are quantified by Rodriguez and Gutierrez[32] and Thomser *et al.*[36] and are reported in Equation (1) and (2).

$$\sigma \,(\text{in MPa}) = \sigma_0 + \Delta\sigma + \alpha \times M \times \mu \times \sqrt{b} \\ \times \sqrt{\frac{1 - \exp(-Mk_r\varepsilon)}{k_r \times L}} \tag{1}$$

where σ and ε are responsible for the von Mises stress and equivalent plastic strain, respectively. The description of each term in Equation (1) is given below and the values, which are used were found from an earlier work.[37] The first term σ_0 takes care of the Peierls stress and effects of alloying elements in the solid solution (Equation 2). Thomser

$$\sigma_0 \,(\text{in MPa}) = 77 + 750 \times (\% \,\text{P}) + 60 \times (\% \,\text{Si}) + 80 \\ \times (\% \,\text{Cu}) + 45 \times (\% \,\text{Ni}) + 60 \times (\% \,\text{Cr}) \\ + 80 \times (\% \,\text{Mn}) + 11 \times (\% \,\text{Mo}) + 5000 \\ \times (\% \,\text{N}_{ss}). \tag{2}$$

The second term, $\Delta\sigma$, provides strengthening by carbon in solution. In the case of ferrite, it is

$$\Delta\sigma \,(\text{in MPa}) = 5000 \times (\% \,\text{C}_{ss}^f) \tag{3}$$

while for martensite it is

$$\Delta\sigma \,(\text{in MPa}) = 3065 \times (\% \,\text{C}_{ss}^m) - 161 \tag{4}$$

where $\% \,\text{C}_{ss}^f$ and $\% \,\text{C}_{ss}^m$ denote the carbon content (in wt%) in ferrite and martensite, respectively.

For bainite, the effect of solid solution carbon strengthening is marginal compared to the effect of dislocation strengthening.[38] So, for bainite, $\Delta\sigma$ is a function of the prior austenite grain size and transformation temperature. The transformation temperature dependency of $\Delta\sigma$ arises from the fact that $\Delta\sigma$ depends on transformation dislocations.[39,40] Decreasing bainitic transformation temperature would increase the amount of transformation dislocation and increase its $\Delta\sigma$ value. Similarly, prior austenite grain size would also influence $\Delta\sigma$ of bainite, as it can influence the bainitic transformation temperature and kinetics.[38,40] According to the research results from Ramazani *et al.*,[41] $\Delta\sigma$ of bainite in this work can be calculated as Equation (5). They obtained the micro hardness map of the bainitic heat affected zone (HAZ) in gas metal arc (GMA) welded DP600 steel and the results showed that the average hardness in the bainitic region is equal to the hardness of the base DP material that consists of ferrite and martensite. Based on these experimental findings, the hardness of bainite has been considered to be the average hardness of ferrite and martensite following a mixture rule. Furthermore, there is a general direct relationship between
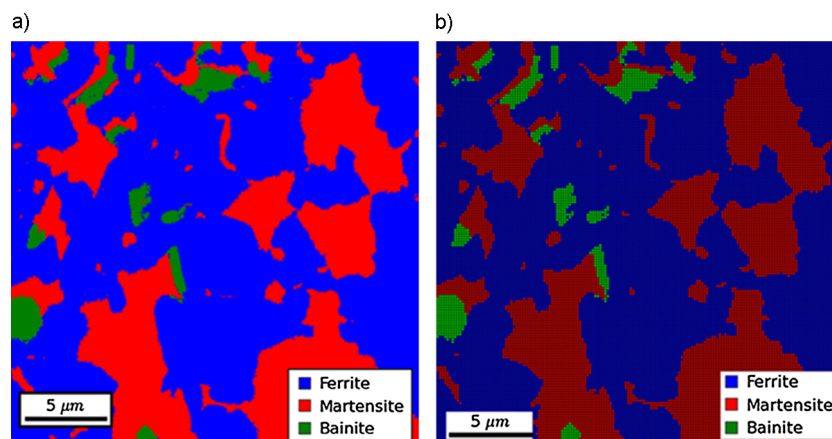

Fig. 6. (a) Final segments of the microstructure and (b) the generated RVE.

ADVANCED ENGINEERING MATERIALS

A. Ramazani et al./Characterization and Modeling of Failure Initiation ...

FULL PAPER

Table 2. Values of parameters used for Micress simulation of intercritical annealing.

Parameters	Value used
Ferrite–austenite interfacial energy	$0.4 \, \mathrm{J \, m^{-2}}$
Ferrite–austenite interface mobility	$1.5 \times 10^{-6} \times \exp(-140\,000/8.314T) \, \mathrm{m^4 \, J^{-1} \, s^{-1}}$
Grid spacing	$0.2 \, \mu\mathrm{m}$
Interface thickness	$1 \, \mu\mathrm{m}$

Table 3. The dislocation mean free path, L, and the recovery rate, k_r, parameters used for calculation of the flow curves of the ferrite, martensite, and bainte phases in DP steel.

Phase	L [m]	k_r [m^{-1}]
Ferrite	d_α	$10^{-5}/d_\alpha$
Martensite	3.8×10^{-8}	41
Bainite	2×10^{-7}	$10^{-5}/d_\gamma$

hardness and strength especially in ductile materials. Based on this observation, we apply the following mixture of rules to identify the $\Delta\sigma$ for bainite in the weld pool or heat-affected zone as a function of $\Delta\sigma_f$ for ferrite and $\Delta\sigma_m$ martensite in the base material (Equation 5):

$$\Delta\sigma_B (\text{in MPa}) = \Delta\sigma_f \times V_f + \Delta\sigma_m \times V_m \qquad (5)$$

where V is the volume fraction of phases.

The last term in Equation (3) is the strain-dependent part. It is deduced from the literature,[37,42] where M_T is the Taylor factor ($M_T = 3$); μ is the shear modulus ($\mu = 80\,000 \, \mathrm{MPa}$); b is the Burger's vector ($b = 2.5 \times 10^{-10}$ m); α is a constant ($\alpha = 0.33$); L is the dislocation mean free path: for ferrite, it is the average grain diameter (d_α), which was determined experimentally, and for martensite, it is 3.8×10^{-8} m.[42] The dislocation mean free path for bainite is assumed to be the average distance between low angle grain boundaries on random directions. The bainitic laths are generally $0.2 \, \mu\mathrm{m}$ in width.[43] Therefore, L is considered as 2×10^{-7} m in this study. k_r is the recovery rate: for ferrite, it is $10^{-5}/d_\alpha$ and for martensite, it is 41.[42] This term is considered to be $10^{-5}/d_\gamma$, where d_γ is the prior austenite grain size. As using the bainitic ferrite lath width in a Hall–Petch equation gives much too high a strength contribution, using the prior austenite grain size seems to give more reasonable values.[40,44,45] Consequently, the recovery rate of bainite in multiphase steels can be estimated as a function of prior austenite grain size. Therefore, the prior austenite grain size should be identified. For this

purpose, the prior austenite grain size was identified by modeling the microstructure of the studied steel in the intercritical annealing temperature (760 °C) using Micress software. The parameters used in Micress and their values were obtained from literature.[46,47] They are summarized in Table 2.

The heating rate to the intercritical annealing temperature was a two-step procedure. In step one; the heating rate was $10 \, °\mathrm{C \, s^{-1}}$ to 680 °C. This was followed by a slower heating rate of $1 \, °\mathrm{C \, s^{-1}}$ to 760 °C. The intercritical annealing time was 2 min. The simulated microstructure is demonstrated in Figure 7. Afterwards, the austenite grain size was determined by the ASTM E12 standard. By following this procedure, the austenite grain size was identified as $12 \, \mu\mathrm{m}$.

The dislocation mean free path, L, and the recovery rate, k_r, for ferrite, martensite, and bainite are also reported in Table 3.

3.3. Extended Finite Element Method (XFEM) and Parameters Identification

Cleavage fracture is defined as the rapid propagation of a crack along a defined crystallographic plane. It often occurs at low temperature and is activated when the first principal stress reaches the cleavage fracture stress. Thus, to perform numerical modeling of cleavage fracture, a stress-based criterion has been applied. Moreover, according to the conventional finite element method, the modeling of crack or failure depends on the use of mesh being conform to geometric discontinuities. Consequently, conventional approach in FE simulation of fracture in material requires mesh refinement. Therefore, the FE results of crack initiation and crack growth are strongly mesh-dependent. To ease this problem, the XFEM, which also allows the application of stress-based criteria, was introduced.[48,49] The principle of XFEM is to deploy a local enrichment of approximated spaces through the partition of the unity concept into finite element approximation. With special enriched function combined with additional degree of freedom, the presence of discontinuity is possible. This enrichment functions consist of the near-tip asymptotic functions, which take the singularity around the crack tip and a discontinuous function that represents the jump in displacement across the crack surfaces into account. Then, the approximation for a displacement vector function, u by partitioning the unity enrichment is
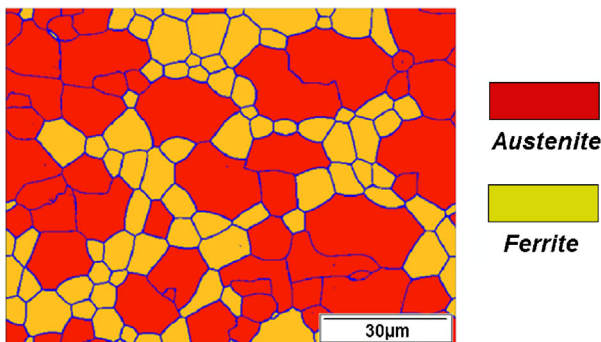

Fig. 7. Simulated MICRESS microstructure at intercritical annealing for 2 min at 760 °C.

A. Ramazani et al./Characterization and Modeling of Failure Initiation ...
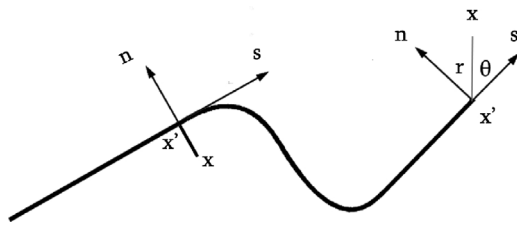
ADVANCED ENGINEERING MATERIALS

FULL PAPER

Fig. 8. Normal and tangential coordinates for a smooth crack.[51]

defined as:[48,49]

$$u = \sum_{I=1}^{N} N_I(x)\left[u_I + H(x)a_I + \sum_{\alpha=1}^{4} F_\alpha(x)b_I^\alpha\right] \quad (6)$$

with $N_I(x)$, usual nodal shape function; u_I, usual nodal displacement vector associated with the continuous part of the finite element solution; $H(x)$, discontinuous jump function across the crack surface; a_I, product of the nodal enriched degree of freedom vector; $F_\alpha(x)$, elastic asymptotic crack-tip functions; b_I^α, product of the nodal enriched degree of freedom vector.

The first term in Equation (6) is applied to all the nodes while the second term is valid for nodes in which shape function support is cut by the crack interior and the third term is applied only to nodes whose shape function support is cut by the crack tip. Figure 8 illustrates the discontinuous jump function across the crack surface, $H(x)$, which is defined by;[50–52]

$$H(x) = \begin{cases} 1 & \text{if} & (x-x^*)\,n \geq 0 \\ -1 & \text{otherwise} \end{cases} \quad (7)$$

with x, sample Gauss point; x^*, point on the crack closest to x; n, unit outward normal to the crack at x^*. Furthermore, Figure 8 also shows the asymptotic crack tip functions in an isotropic material, $F_\alpha(x)$, which is given as;[49,51]

$$F_\alpha(x) = \left[\sqrt{r}\sin\frac{\theta}{2}, \sqrt{r}\cos\frac{\theta}{2}, \sqrt{r}\sin\theta\sin\frac{\theta}{2}, \sqrt{r}\sin\theta\cos\frac{\theta}{2}\right] \quad (8)$$

with (r, θ) is a polar coordinate system with its origin at the crack tip.

The damage onset and progression were modeled with the so-called cohesive segments method in conjunction with phantom nodes.[50,52] The phantom nodes or superposed original real nodes were utilized to represent the discontinuity of cracked elements. When an element is intact, the phantom nodes are constrained to their corresponding real nodes. But when a crack cuts through the element, a part is formed consisting of the real nodes and a phantom node depending on the orientation of the crack. The principle of the phantom nodes is shown in Figure 9. For controlling the magnitude of separation with XFEM, cohesive law was defined. A separation occurs when cohesive strength of cracked elements reaches zero. To define a set of full interpolation bases, part of cracked element belonged in the real domain, Ω_0, is extended to the phantom node, Ω_P. With the integration over the area from the side of the real nodes up to the crack; i.e., Ω_0^+ and Ω_0^-, the jump in the displacement field is possible. This XFEM-based cohesive segments method can be used to simulate crack initiation and propagation along an arbitrary, solution-dependent path in the bulk materials, since the crack propagation is not tied to the element boundaries in a mesh. With this approach, the near-tip asymptotic singularity is not required and only the displacement jump across a cracked element is considered. Hence, the approximation for a displacement vector function with the partition of unity enrichment is deducted to:[52]

$$u = \sum_{I=1}^{N} N_I(x)[u_I + H(x)a_I] \quad (9)$$

For the combination between cohesive segments method and XFEM, a TSL is implemented. The appropriate shape of the TSL for brittle material is shown in Figure 10. To define the TSL, the maximum cohesive stress and a suitable damage evolution law for degradation of material stiffness must be identified. In this work, the maximum principal stress criterion (MAXPS) is used for describing damage initiation. The brittle material is assumed to lose its stiffness as soon as the damage initiation criterion is reached and linear degradation behavior with steep slope is assigned as damage evolution law.

The maximum principle stress criterion (MAXPS) using critical failure stress (σ_c) and failure energy (E_c) is applied to
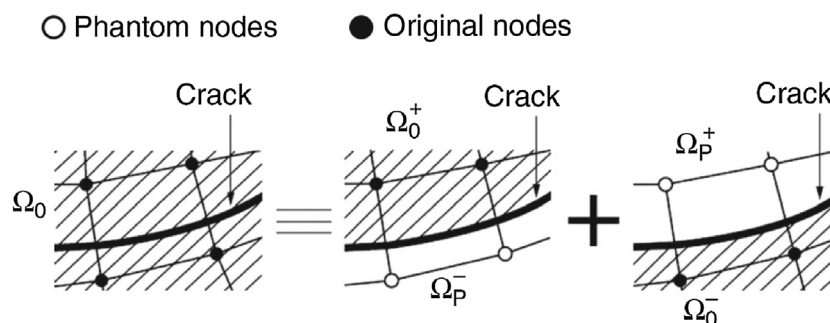

Fig. 9. Usage of XFEM by implementation of phantom nodes.

ADVANCED ENGINEERING MATERIALS

A. Ramazani et al./Characterization and Modeling of Failure Initiation ...
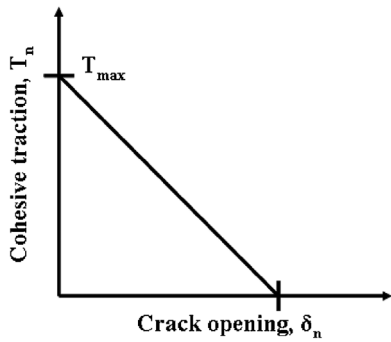
FULL PAPER

Fig. 10. Traction–separation law with maximum principal stress as criterion for crack initiation and linear softening behavior.

describe damage initiation. Martensite is assumed to lose its stiffness as soon as the damage initiation criterion is reached and linear degradation behavior with steep slope is assigned as local damage evolution law on mesoscale.[19–21,53] For this purpose, the correspondent local strain for failure initiation in DP steels in mini tensile tests with DIC technique was first determined.[20,53] Micromechanical modeling based on 2D RVE calculations was performed in order to identify the average equivalent strain in martensite when the crack initiation occurs. Therefore, the simulations were conducted up to the determined local failure strains from the experiments. Then, using first order homogenization strategy,[54] average equivalent plastic strain in martensite was calculated. The correspondent stress for this strain can be considered as critical stress for martensite cracking, σ_c, and it was calculated from the flow curve of martensite according to fracture toughness theory,[55,56] critical failure energy for martensite failure, E_c, was calculated from the martensite stress–strain curve.

3.4. Correlation Between 2D and 3D Flow Curve Modeling

Since real specimen deforms three-dimensionally, 2D modeling approaches cannot predict the flow curve of the material precisely. The predicted flow curves obtained from 2D modeling should be correlated to the 3D ones by introducing a correlation factor. Ramazani et al.[31] quantified the stress ratio (σ_{3D}/σ_{2D}) based on the 2D and 3D RVE calculations for DP600 steels with various martensite phase fractions ($V_m = 0$–50%) at different equivalent plastic strains varying from $\varepsilon_{eq}^{P} = 0 - 0.1$. The developed correlation factor is a polynomial equation containing terms for both the martensite fraction and the equivalent plastic strain (Equation 10). The elaborated details are given in ref.[31]

$$
\begin{aligned}
\frac{\sigma 3D}{\sigma 2D} =\ & 2 \times 10^{-4} \times (\varepsilon_{eq}^{P})^2 \times V_m^3 - 1 \times 10^{-7} \times (\varepsilon_{eq}^{P}) \times V_m^3 \\
& + 1 \times 10^{-7} \times V_m^3 + 0.0218 \times (\varepsilon_{eq}^{P})2 \times V_m^2 \\
& - 0.0015 \times (\varepsilon_{eq}^{P}) \times V_m^2 + 7 \times 10^{-5} \times V_m^2 + 0.18 \\
& \times (\varepsilon_{eq}^{P})2 \times V_m + 0.007 \times (\varepsilon_{eq}^{P}) \times V_m + 0.0036 \\
& \times V_m \times (\varepsilon_{eq}^{P})^2 + 1\sqrt{2}
\end{aligned}
\tag{10}
$$

As Equation (10) was already validated for different industrial DP steels, it was used to correlate the predicted 2D flow curve to a 3D flow curve. Because the percentage of bainite (third phase) in the material is low (5%), this developed correlation factor for DP steel with two phases is applicable. More details can be found in ref.[40]

4. Results and Discussions

4.1. Microstructure Characterization

Compared to ferrite, bainite normally has more dislocations and therefore, to distinguish it Kernel average misorientation (KAM) is needed. However, in DP steels, distinguishing is even more complex since transformation-induced geometrically necessary dislocation (GND) zones around martensite islands. Therefore, the EPMA carbon intensity map is combined with KAM to finally identify the bainite areas. The regions with high misorientation (>0.5°) and containing carbon content are assigned to bainite. The Figure 11a shows the KAM result from the EBSD mapping without the martensite islands and the Figure 11b shows the EPMA carbon intensity map in which the martensite and
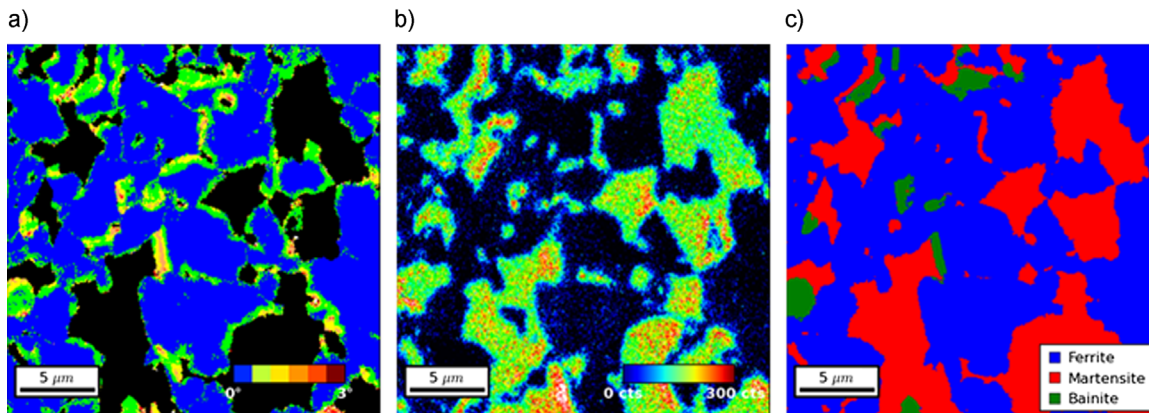

Fig. 11. (a) EBSD mapping showing the KAM (step size: 100 nm, kernel radius: 300 nm) without the identified martensite grains and (b) EPMA carbon intensity map (step size: 100 nm, dwell time: 100 ms). (c) The final segment of the microstructure.[3]
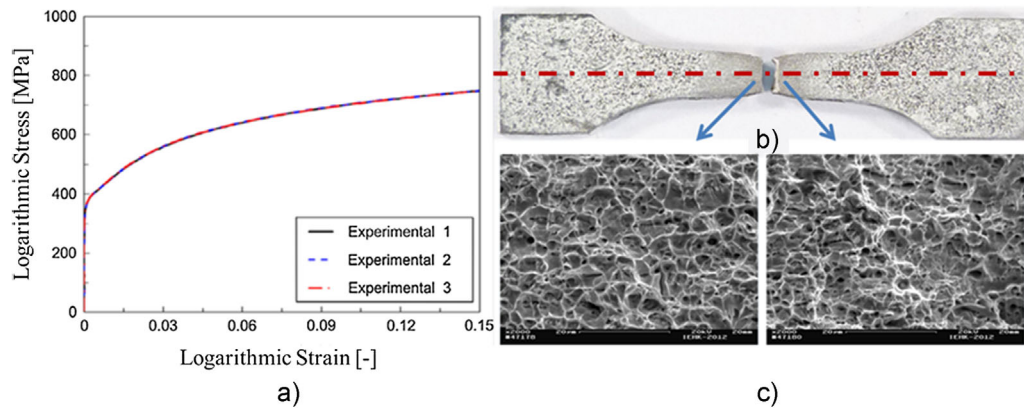
Fig. 12. (a) The experimental true stress--true strain curve (b) the broken sample after uniaxial tensile test and (c) the corresponding fracture surface.

bainite area are highlight. Figure 11c represents the corresponding final segment of bainite-aided DP steel. Combining EBSD and EPMA, martensite covers 30% of the measured area, while bainite covers just 5% of this area. A detailed description of the data could be found in ref.[26]

According to the results of EPMA measurement, carbon and manganese were estimated to be 0.72 and 1.56 wt% in a martensite, respectively. However, manganese concentration was found to be similar in bainite as 1.60 wt%.[26,40] According to carbon solubility in iron, the carbon concentration in ferrite was considered as 0.004 wt%. The concentration of the other elements was found to be homogeneous in all phases; the nominal concentration was used in the modeling.[40]

4.2. Uniaxial Tensile Test and Fractography

Figure 12a shows the experimental flow curves of three parallel tensile tests on the studied DP steel. Small, but still existing scatter can be found what fits well with the expectations for this steel quality.
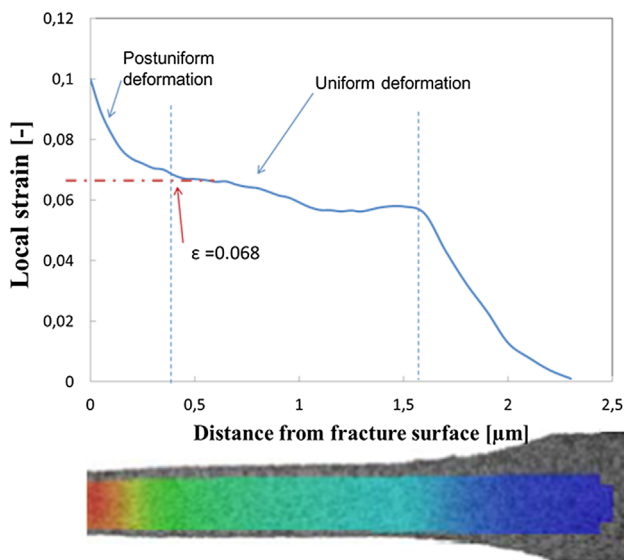
Figure 12b shows the top of a failed specimen under uniaxial tension. The side view of the localized area of the sample shows a shear failure mode where the fracture surfaces are inclined almost at 45° with respect to the loading direction. Red line in Figure 12b shows the cutting line for microstructural investigation. SEM images were taken along this line on the thickness direction. Here, the deformation in the top view can be considered to be under a plane stress loading condition since the thickness of the specimen is much less than the width and the mesoscale of simulation is reasonable smaller than the macroscale of tensile specimen.[17] Therefore, the RVE for tensile modeling as shown in Figure 6 was modeled with plane stress elements (CPS4R) to simulate the failure mode in the material.

Figure 12c shows the fracture surface of tensile specimen. The micrographs reveal the ductile fracture modes of the steels. This suggests a failure process of void nucleation and growth.

4.3. Mini Tensile Test with DIC Technique Evaluation and XFEM Parameters Identification

Mini tensile test was carried out and analyzed using DIC technique to investigate the microstructural evolution during

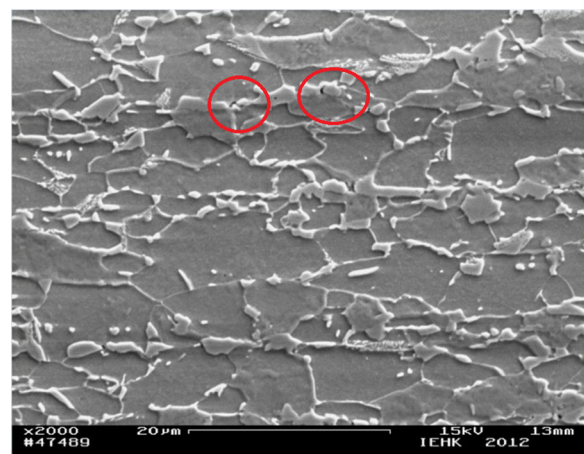Fig. 13. Local strain distributions along central line during loading direction on DP steel.

Fig. 14. SEM image in centerline of broken tensile specimen at failure position.
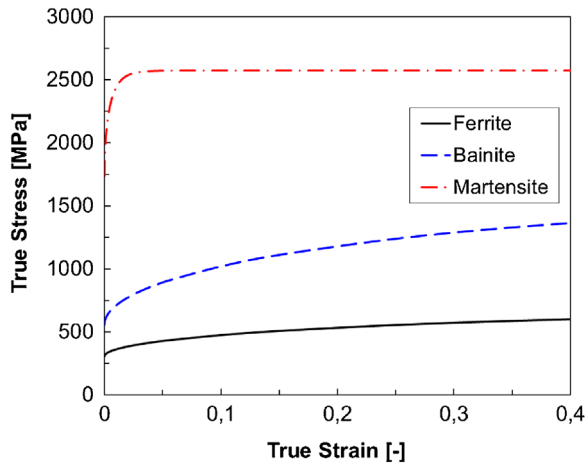
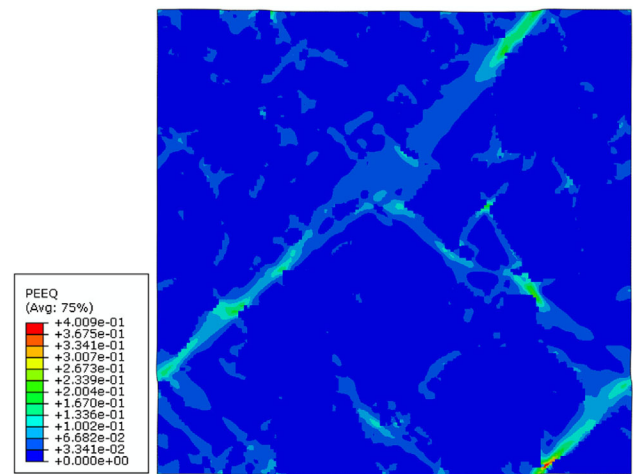Fig. 15. Flow curves of the single phases in bainite-aided DP steel.

Fig. 17. Equivalent strain of the RVE at macroscopic local failure strain from experiments ($\varepsilon_f = 0.068$).

tensile test and to quantify the local strain along the tensile axis. Combining these local strain values with the SEM analysis along the center line allows the matching of failure initiation position and local strain in the center of deformed specimen. During tensile test, images were taken at the surface in every second. Then, strain distributions can be captured in different deformation steps in the evaluated zone, as shown in Figure 13.

After tensile test, the broken samples showed visibly necking near the fracture surface because the width and thickness decreased while the specimens were elongated. Thus, the facture mode in DP steel is ductile and it should be identified where the micro crack starts. For this purpose, surfaces perpendicular to the fracture surface were also analyzed.

Figure 14 shows the microstructure evolution by means of SEM in the center line along loading direction in the

investigated DP steel where the crack initiates. As can be observed in this figure, the failure initiation occurs in martensite. Furthermore, from Figure 13 and 14, the local strain at failure initiation position in tensile was estimated as $\varepsilon_f^t = 0.068$. This value is used to identify the parameters for failure initiation modeling.

4.4. Flow Curve of Single Phase

Calculated single phase flows curves of ferrite, martensite, and bainite for studied bainite-aided DP steel, as described in Section 3.2, are depicted in Figure 15. Ferrite shows lowest strength while martensite presents the highest strength. No work hardening can be seen in the martensite flow curve after approximately 0.02 true strain. The flow curve of bainite is located in between those of ferrite and martensite. Bainite possesses the highest work hardening in comparison to the other phases.
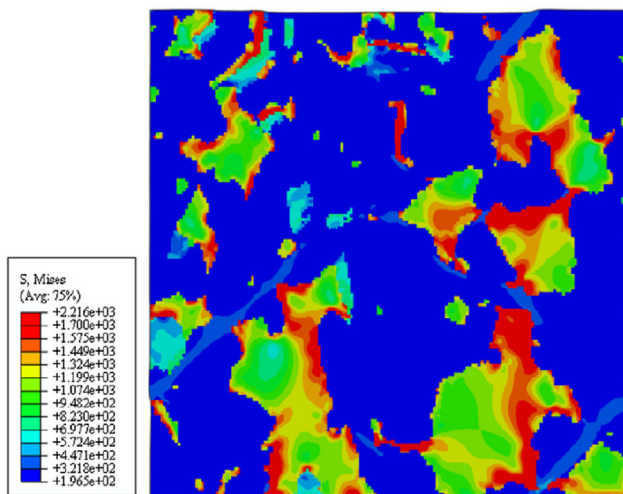

Fig. 16. Von Mises stress of the RVE at macroscopic local failure strain from experiments ($\varepsilon_f = 0.068$).
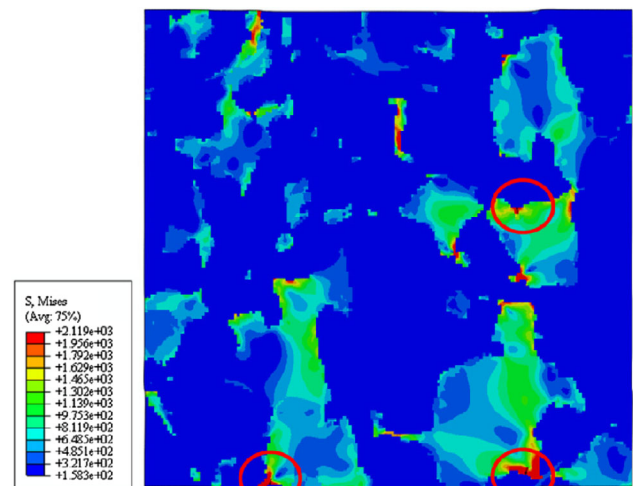

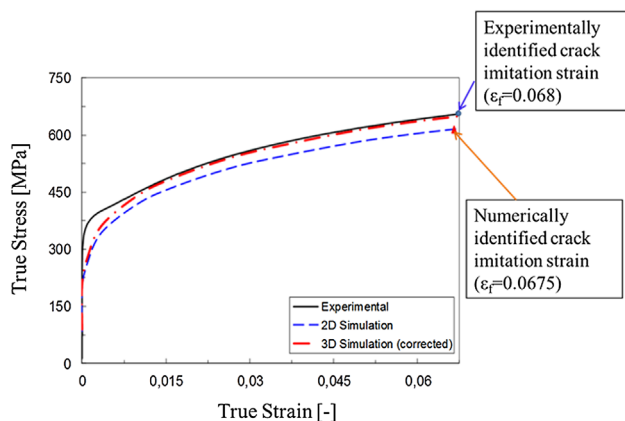Fig. 18. Von Mises stress distribution of bainite-aided DP steel.

Fig. 19. The comparison of the experimental and simulation flow curves (the blue dot indicates the experimental failure point and the red triangle indicates the simulation failure point).

4.5. XFEM Parameter Identification

The corresponding local failure initiation strain in the studied bainite-aided DP steel in mini tensile tests with DIC technique was first determined as $\varepsilon_f^t = 0.068$. To identify the equivalent crack initiation strain in martensite $\varepsilon_{f,m}$, 2D RVE micromechanical modeling was performed until macroscopic failure initiation state $\varepsilon_f^t = 0.068$. Figure 16 and 17 illustrate the contour plot of von Mises stress and equivalent plastic strain on mesoscale at ε_f^t, respectively. While the hard martensite carries stresses of more than 2200 MPa, the ferrite shows much lower stresses. On the other hand, martensite undergoes small plastic strain while the development of shear bands is observed in ferrite. These bands of localized plastic strain in ferrite are observed at 45° to the tensile direction and they might probably be over predicted because of the plane stress condition. It is worth to be mentioned that martensite undergoes finite plastic strains in all cases what is in line with experimental findings in literature.[57–59]

Based on these results, the corresponding average equivalent plastic strain in martensite was calculated to be $\varepsilon_{f,m} = 0.018$ using first order homogenization strategy.[48] The correspondent stress for this strain can be considered as critical stress for martensite cracking and it was calculated from the flow curve of martensite ($\sigma_c = 2119$ MPa). Critical energy (E_c) for martensite failure was considered as the area of below martensite stress–strain curve and calculated as $E_c = 12.6$ J m^{-2}.[53,55,56] The developed failure parameters are applied in XFEM to simulate the crack initiation.

4.6. Modeling of Failure in DP Steels Using XFEM

The initiation of cracks in quasi-static problems is studied using XFEM. Numerical tensile tests were carried out on the generated 2D RVEs of DP steel. The evolution of stress and strain in the RVEs can be obtained from these numerical tensile tests.

Figure 18 shows the contour plot of von Mises stress and damage evolution on microscale at $\varepsilon_f^b = 0.068$. A comparison

between experimental and predicted true stress--true strain curves from 2D RVE calculations is demonstrated in Figure 19. Also, the corrected 2D flow curve to 3D flow curve is shown using correlation factor as explained in Section 3.4. It can be seen, that the corrected 3D flow curve is in good agreement with the experimental flow curve in both conditions. Comparison between experimental and simulated flow curves reveals that the simulations show roughly the same crack initiation strain as experiments.

5. Summary and Conclusions

Martensite cracking has been identified to be the main failure initiation mechanisms in the bainite-aided DP steel. Mini tensile test with DIC technique offers the quantification of martensite failure initiation as function of macroscopic loading. Quantitative identification of parameters for XFEM modeling of martensite cracking has been performed and validated by numerical versus experimental tensile test comparison. Comparison between experimental and simulated flow curves shows good agreement.

[1] P. Tsipouridis, *PhD Thesis*, TU Munchen, Germany **2006**.
[2] R. Khamedi, A. Fallahi, H. Zoghi, *Int. J. Recent Trend. Eng.* **2009**, *1*(5), 30.
[3] A. Ramazani, B. Berme, U. Prahl, in *Structural Materials and Processes in Transportation* (Eds: D. Lehmhus, M. Busse, A. S. Herrmann, K. Kayvantash), Wiley-VCH, Weinheim, Germany **2013**, p. 5.
[4] M. Sudo, T. Iwai, *ISIJ Int.* **1983**, *23*, 294.
[5] I. Kim, S. Raiachel, W. Dahl, *Steel Res.* **1987**, *58*, 186.
[6] D. K. Matlock, G. Krauss, *Mater. Sci. Eng. A* **1995**, *165*, 1.
[7] M. Sarwar, R. Priestner, *J. Mater. Sci.* **1996**, *31*(8), 2091.
[8] H. P. Shen, T. C. Lei, J. Z. Liu, *Mater. Sci. Technol.* **1986**, *2*, 28.
[9] L. Steinbrunner, D. K. Matlock, G. Krauss, *Metall. Mater. Trans. A* **1988**, *19*, 579.
[10] Y. L. Su, J. Gurland, *Mater. Sci. Eng.* **1987**, *95*, 151.
[11] A. Güral, S. Tekeli, T. Ando, *J. Mater. Sci.* **2006**, *41*(23), 7894.
[12] E. Maire, O. Bouaziz, M. D. Michiel, C. Verdu, *Acta Mater.* **2008**, *18*, 4954.
[13] M. S. Rashid, *Conference Proceedings, Met. Soc. of AIME*, Chicago, USA **1979**, p. 1.
[14] X. J. He, N. Terao, A. Berghezan, *Metal Sci.* **1984**, *18*, 367.
[15] N. J. Kim, G. Thomas, *Metall. Trans. A* **1981**, *12*, 483.
[16] M. Calcagnotto, Y. Adachi, D. Ponge, D. Raabe, *Acta Mater.* **2011**, *59*(2), 658.
[17] X. Sun, K. S. Choi, W. N. Liu, M. A. Khaleel, *Int. J. Plast.* **2009**, *25*, 1888.

[18] K. S. Choi, W. N. Liu, X. Sun, M. A. Khaleel, *Metall. Mater. Trans. A* **2009**, *40*, 796.

[19] V. Uthaisangsuk, U. Prahl, W. Bleck, *Proc. Eng.* **2009**, *1*(1), 171.

[20] N. Vajragupta, V. Uthaisangsuk, B. Schmaling, S. Münstermann, A. Hartmaier, W. Bleck, *Comput. Mater. Sci.* **2012**, *54*, 271.

[21] A. Ramazani, A. Schwedt, A. Aretz, U. Prah, W. Bleck, *Comput. Mater. Sci.* **2013**, *75*, 35.

[22] A. Ramazani, A. Schwedt, A. Aretz, U. Prahl, *Key Eng. Mater.* **2014**, *586*, 67.

[23] A. Ramazani, M. Abbasi, U. Prahl, W. Bleck, *Comput. Mater. Sci.* **2012**, *64*, 101.

[24] X. Sun, K. S. Choi, A. Soulami, W. N. Liu, M. A. Khaleel, *Mater. Sci. Eng. A* **2009**, *526*, 140.

[25] G. Avramovic-Cingara, Y. Ososkov, M. K. Jain, D. S. Wilkinson, *Mater. Sci. Eng. A* **2009**, *516*, 7.

[26] P. T. Pinard, A. Schwedt, A. Ramazani, U. Prahl, S. Richter, *Microsc. Microanal.* **2013**, *19*, 996.

[27] N. McCormick, J. Lord, *Method. Mater.* **2010**, *13*, 52.

[28] ARAMIS Benutzerhinweise v5.4.1, *Gesellschaft für Optische Messtechnik*, **2005**.

[29] L. Yang, L. Smith, A. Gothekar, X. Chen, Technical Report, Oakland University, **2010**.

[30] A. Ramazani, K. Mukherjee, U. Prahl, W. Bleck, *Comput. Mater. Sci.* **2012**, *52*, 46.

[31] A. Ramazani, K. Mukherjee, H. Quade, U. Prahl, W. Bleck, *Mater. Sci. Eng. A* **2013**, *560*, 129.

[32] R. M. Rodriguez, I. Gutierrez, *Mater. Sci. Forum* **2003**, *426–432*, 4525.

[33] Y. Bergström, *Mater. Sci. Eng.* **1970**, *5*(4), 193.

[34] Y. Estrin, H. Mecking, *Acta Metall.* **1984**, *32*(1), 57.

[35] J. G. Sevillano, in *Mater. Sci. Technol.: A Comprehensive Treatment, Plastic Deformation and Fracture of Materials*, Vol. *6* (Ed: H. Mughrabi), VCH, Weinheim, Germany **1993**.

[36] C. Thomser, V. Uthaisangsuk, W. Bleck, *Steel Res. Int.* **2010**, *80*(8), 582.

[37] O. Bouaziz, P. Buessler, *La Rev. Métall. – CIT* **2002**, *99*, 71.

[38] H. K. D. H. Bhadeshia, *Bainite in Steels*, 2nd edition, IOM Communications Ltd, London **2001**.

[39] O. Bouaziz, K. Zhu, C. Oberbillig, M. Huang, *Mater. Sci. Eng. A* **2010**, *527*(24–25), 6614.

[40] A. Ramazani, P. Pinard, A. Schwedt, S. Richter, U. Prahl, W. Bleck, *Comput. Mater. Sci.* **2013**, *75*, 35.

[41] A. Ramazani, K. Mukherjee, A. Abdurakhmanov, U. Prahl, M. Schleser, U. Reisgen, W. Bleck, *Mater. Sci. Eng. A* **2014**, *589*, 1.

[42] C. Thomser, *PhD Thesis*, RWTH-Aachen, Germany **2009**.

[43] N. J. Kim, G. Thomas, *Metall. Trans. A* **1981**, *12*, 483.

[44] T. Gladman, D. Dulieu, I. McIvor, *Structure–Property Relationships in High Strength Microalloyed Steels, Microalloying*, Vol. *75*, New York **1977**, p. 32.

[45] J. A. Whiteman, *Low Carbon Steels for the Eighties*, The Institution of Metallurgists, **1977**, *3*(6), I.

[46] J. Rudnizki, B. Böttger, U. Prahl, W. Bleck, *Metall. Mater. Trans. A* **2011**, *42*, 2516.

[47] A. Ramazani, Y. Li, K. Mukherjee, U. Prahl, W. Bleck, A. Abdurakhmanov, M. Schleser, U. Reisgen, *Comput. Mater. Sci.* **2013**, *68*, 107.

[48] J. M. Melenk, I. Babuska, *Comput. Methods Appl. Mech. Eng.* **1996**, *139*, 289.

[49] T. Belytschko, T. Black, *Int. J. Numer. Meth. Eng.* **1999**, *45*, 601.

[50] J. Song, P. Areias, T. Belytschko, *Int. J. Numer. Meth. Eng.* **2006**, *67*, 868.

[51] ABAQUS, *Analysis User's Manual*, Version 6.10, Dassault Systèmes, USA **2010**.

[52] J. Remmers, R. de Borst, A. Needleman, *J. Mech. Phys. Solids* **2008**, *56*, 70.

[53] A. Ramazani, Z. Ebrahimi, U. Prahl, *Comput. Mater. Sci.* **2014**, *87*, 241.

[54] V. G. Kouznetsova, *PhD Thesis*, Technical University Eindhoven, The Netherlands **2002**.

[55] G. E. Dieter, *Mechanical Metallurgy*, 2nd edition, McGraw-Hill, New York, USA **1976**.

[56] R. W. Hertzberg, R. P. Vinci, J. L. Hertzberg, *Deformation and Fracture Mechanics of Engineering Materials*, 5th edition, Wiley **2012**.

[57] M. Azuma, S. Goutianos, N. Hansen, G. Winther, X. Huang, *Mater. Sci. Technol.* **2012**, *28*(9–10), 1092.

[58] A. Ramazani, K. Mukherjee, U. Prahl, W. Bleck, *Metall. Mater. Trans. A* **2012**, *43*, 3850.

[59] A. Ramazani, K. Mukherjee, A. Schwedt, P. Goravanchi, U. Prahl, W. Bleck, *Int. J. Plast.* **2013**, *43*, 128.